Supplementary Information

Co_2P as a pre-catalyst: enhancing NO_3RR activity by controlled surface activation

Paz Stein,[1] Yan Tetarevsky,[1] Yakir Levi-Sagzan,[1] Naor Cohen,[1] Ronen Bar-Ziv,[2*] Maya Bar-Sadan[1*]

[1]*Department of Chemistry, Ben Gurion University, Beer-Sheva, 8410501 Israel.*

[2] *Department of Chemistry, Nuclear Research Center Negev, P.O. Box 9001, Beer-Sheva 84190, Israel*

1. Experimental Section

1.1 Materials

Ammonium chloride (NH_4Cl, 99.5%) was purchased from Acros Organics. Alfa Aesar supplied sodium hypochlorite solution (11–14% available chlorine), sodium nitroprusside dihydrate (≥99%), salicylic acid (99%), trisodium citrate dihydrate (99%), Nafion D-521 dispersion (5 wt%), and cobalt(II) chloride anhydrous (99.7%), cobalt powder (-400 mesh, 99.5% metals basis). Hexadecylamine (90%), sodium nitrite ($NaNO_2$, analysis grade, ≥99%), sodium nitrate-^{14}N (≥99.0%), sodium nitrate-^{15}N (≥98% atomic, ≥99%), sodium chloride (NaCl, 99.5%), and *N*-(1-naphthyl)ethylenediamine dihydrochloride were obtained from Sigma-Aldrich. Sodium dihydrogen phosphate monohydrate (ACS) and disodium hydrogen phosphate dihydrate (ACS) were sourced from Supelco. 1-Octadecene (90%) was purchased from Thermo Fisher Scientific. Dimethyl sulfoxide-d_6 (99.9%) was obtained from Cambridge Isotope Laboratories, Inc. Chloroform, sodium hydroxide, and isopropyl alcohol were supplied by Bio-Lab Ltd., and ethanol was purchased from Romical. Triphenyl phosphite (97%) was obtained from Stern Chemicals. All aqueous solutions were prepared using deionized water purified with a Milli-Q system (resistivity ≥18.2 MΩ·cm).

1.2 Catalyst synthesis

Co_2P nanorods were synthesized via a colloidal route adapted from a reported procedure.[1] In a 100 mL three-neck round-bottom flask, 10 mmol of hexadecylamine were dissolved in 25.34 mL of octadecene. The mixture was heated to 50 °C under continuous vacuum evacuation with

stirring for 0.5 h. Subsequently, 10 mmol of triphenyl phosphite were injected, and the temperature was increased to 60 °C and maintained under vacuum for an additional 0.5 h. Separately, 1 mmol of anhydrous $CoCl_2$ was dispersed in 2 mL of ethanol. The resulting solution was rapidly injected into the reaction flask, which had been continuously purged with N_2. The temperature was gradually raised to 150 °C and held for 1 h to remove ethanol and ensure an inert environment. After this step, the system was maintained under a continuous N_2 flow, and the temperature was increased to 270 °C and held for 1 h. Upon completion of the reaction, the heating was switched off, and the flask was allowed to cool slowly to 150 °C before removal from the heating mantle. The obtained powder was collected, washed thrice with a chloroform/isopropanol mixture (1:5, v/v), dried under vacuum, and stored in a glovebox.

1.3 Characterization methods

Transmission electron microscopy (TEM) images were captured using a Tecnai T12 G2 TWIN Thermo Fisher transmission electron microscope. The sample was prepared by dissolving a small amount of catalyst powder in ethanol, ultrasonicating for 15 minutes, then drop casting 20 μL onto a Cu grid (300 mesh, TED PELLA, INC).

X-ray diffraction (XRD) measurement was carried out using a Rigaku XtalLAB Synergy single crystal X-ray diffractometer, equipped with a Pilatus detector and a standard Cu Kα X-ray source (λ = 1.51418 Å).

X-ray photoelectron spectroscopy (XPS) analysis was conducted using an ESCALAB 250 spectrometer in an ultrahigh vacuum environment (1×10^{-9} bar), equipped with an Al Kα X-ray source and a monochromator.

Mechanistic study by ATR-IRRAS (Attenuated total reflectance-infrared reflection absorption spectroscopy) measurements: In situ ATR analysis was performed using a Thermo Nicolet iS50 FTIR spectrometer equipped with a liquid-nitrogen-cooled MCT-A detector. A circular CaF_2 disc (4000-800 cm^{-1}) served as both the ATR crystal and IR window. The crystal was mounted on a VeeMAX III ATR accessory (PIKE Technologies), integrated with a custom-designed spectro-electrochemical cell using the Otto geometry to allow simultaneous electrochemical control and infrared data collection. The working electrode was a glassy carbon disk onto which the catalyst was drop-cast as a suspension in isopropyl alcohol with Nafion binder. This coated electrode was pressed firmly against the CaF_2 window using an O-ring to ensure optimal optical contact and seal the thin-layer cell. The setup employed a three-

electrode system, featuring an Ag/AgCl (saturated KCl) reference electrode and a platinum foil counter electrode, all governed by a BioLogic SP-300 potentiostat. The electrolyte solution consisted of phosphate-buffered saline (PBS) with sodium nitrate ($NaNO_3$), with concentration adjusted per experiment. Before measurement, the electrolyte was purged with argon for at least 20 minutes and continuously flowed through the cell at 15 mL/min via a peristaltic pump. Background spectra were recorded prior to applying any potential. Infrared spectra were collected in the 1100-4000 cm^{-1} range under various electrochemical conditions, including open-circuit voltage (OCV), no applied potential, and during chronoamperometry at selected reduction potentials.

1.4 Electrochemical measurements

Electrochemical measurements were conducted on a BioLogic VSP workstation using a two-compartment H-cell separated by a Nafion 117 membrane. An Ag/AgCl electrode in saturated KCl served as the reference electrode, a 1×1 cm^2 Pt plate was used as the counter electrode, and a catalyst-coated glassy carbon electrode (diameter: 3 mm) was employed as the working electrode, unless otherwise specified. The catalyst ink was prepared by dispersing 1 mg of Co_2P powder and 1 mg of Vulcan carbon black in a mixture of 200 μL deionized water, 200 μL isopropanol, and 14 μL Nafion solution. The suspension was sonicated for 30 min to obtain a homogeneous ink, and a 15 μL aliquot was drop-cast onto the glassy carbon electrode, yielding a catalyst loading of ~0.5 mg cm^{-2}. All electrochemical nitrate reduction reactions were performed in 0.1 M phosphate-buffered saline (PBS) containing 1 M $NaNO_3$ (pH 6.7). All potentials were corrected for ohmic resistance with 100% iR compensation. Before measurements, the electrolyte was purged with Ar gas for at least 15 min. During measurements, the cathodic compartment was continuously stirred with a magnetic stirrer.

In this study, all potentials were referenced to a reversible hydrogen electrode (RHE) and are reported with 100% iR compensation, following the equation:

$$E_{RHE} = E_{(Ag|AgCl)} + E^0_{(Ag|AgCl\ )} + 0.059 \cdot pH$$

The standard reference electrode potential, $E^0_{Ag|AgCl\ (sat.KCl)}$, was 0.197 V, and a calibrated pH meter was used to measure the electrolyte's pH value.

The Faradaic efficiency for NH_3 and NO_2^- was determined using the following equation:

$$FE = \frac{z \cdot C_{product} \cdot V_{half\ cell} \cdot F}{Q_{applied}} \times 100\%$$

Where z represents the number of electrons transferred during the reaction (8 e^- for NH_3, 2 e^- for NO_2^-), $C_{product}$ is the concentration of the product in the electrolyte (mol L^{-1}), $V_{half\ cell}$ refers to the electrolyte volume of the cathodic half-cell (0.035 L), F is Faraday's constant (96,485 C mol^{-1}), and Q applied indicates the applied charge during the chronoamperometric measurement (C).

The yield rates of NH_3 production were calculated by:

$$r_{NH_3} = \frac{C_{NH_3} \cdot V_{half-cell}}{t \cdot n_{catalyst}}$$

Where t represents the duration of the chronoamperometric measurement in hours, and $n_{catalyst}$ denotes the catalyst loading in milligrams.

Potentiostatic electrochemical impedance spectroscopy (PEIS) measurements were performed at an applied potential of -0.5 V vs RHE over a frequency range from 100 kHz to 100 mHz using an AC perturbation amplitude of 10 mV. The impedance data were fitted and simulated using the EC-Lab software (BioLogic) based on an equivalent circuit consisting of a solution resistance (R_1) in series with a parallel combination of charge-transfer resistance (R_2) and a constant phase element (Q_2).

Long-term stability measurements were performed for the Co_2P/Co catalyst at -0.55 V vs. RHE, corresponding to the potential where the catalyst exhibited high NH_3 yield rate and Faradaic efficiency. The experiment was conducted using a circulating catholyte configuration, in which the cathodic compartment was continuously circulated with a total electrolyte volume of 500 mL throughout the reaction. The electrolyte was continuously purged with Ar and stirred during electrolysis. The measurement was paused three times during the 24 h test to collect electrolyte aliquots for product quantification, after which electrolysis was resumed.

2. Surface activation of Co_2P (Co_2P/Co preparation)

The Co_2P catalysts were activated through a two-step procedure adapted from a reported CoP treatment.[2] For reference, the pristine Co_2P surface is shown in **Figure S1** (top panel), which displays the Co-P peak along with minor Co-O presence. The first activation step involved immersing the Co_2P-coated electrode in 1 M KOH for 10 minutes, which generated a $Co(OH)_2$ surface. The corresponding Co 2p spectrum (**Figure S1,** middle panel) shows a dominant oxidation feature at 780.9 eV accompanied by a broad satellite peak at 786.2 eV, matching the characteristic XPS profile of $Co(OH)_2$ (denoted as oxidized Co and sat.).[3] Immediately afterward, the electrode was transferred to a three-electrode electrochemical cell containing 1 M KOH, where a reduction potential of -0.6 V vs. RHE was applied for 5 minutes. After this reduction step (**Figure S1**, bottom panel), the reduced Co/covalent Co-P/$Co^{\delta+}$ peak reappears, and the hydroxide-related satellite features diminish, while the oxidized Co-associated envelope becomes more pronounced. This indicates that the hydroxide layer is only partially reduced, with a fraction of the surface cobalt remaining oxidized. Overall, the activation procedure produces a transient hydroxide-rich cobalt surface that is partially reduced under cathodic bias, leading to a reduced cobalt-rich Co_2P/Co surface. Because the Co 2p region contains overlapping contributions from metallic Co and covalent Co-P environments, the assignment is made based on the full activation sequence, the similarity to the reported CoP → $Co(OH)_2$ → CoP@Co transformation, and the accompanying electrochemical enhancement, rather than on Co 2p XPS alone.[2]

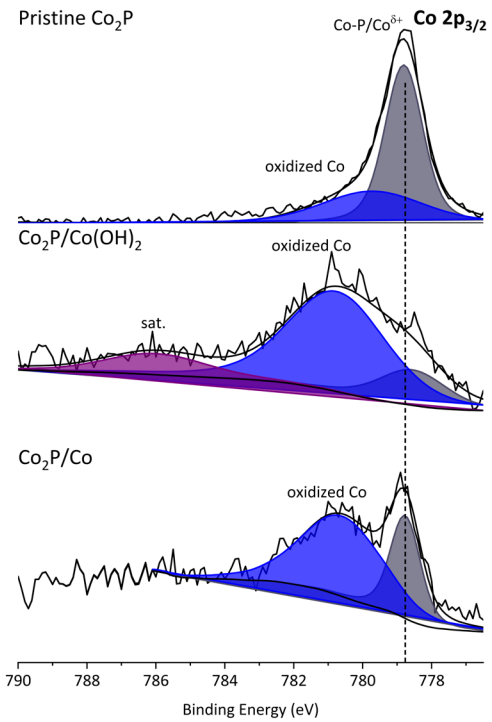

Figure S1. High-resolution Co $2p_{3/2}$ XPS spectra of Co_2P at different activation stages: pristine Co_2P (top), $Co(OH)_2$ surface intermediate formed after immersion in 1 M KOH (middle), and Co_2P/Co surface obtained after electroreduction at -0.6 V vs. RHE (bottom)

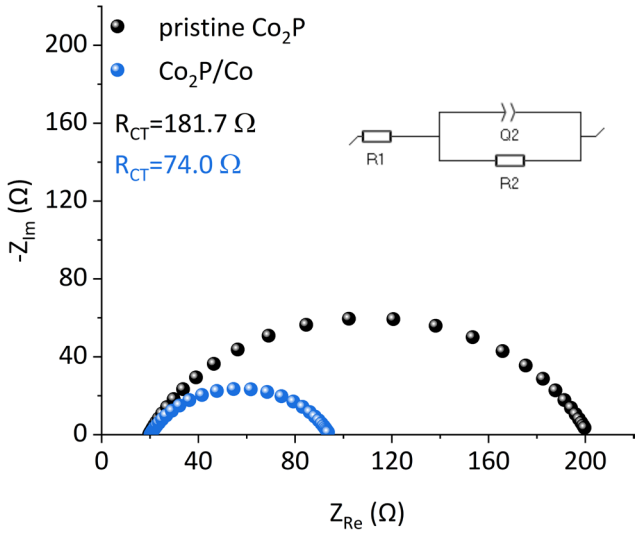

Figure S2. Electrochemical impedance spectroscopy Nyquist plots for the pristine Co_2P and the Co_2P/Co samples, measured at -0.5 V vs. RHE.

3. Colorimetric measurements

Colorimetric measurements were performed with a SHIMADZU UV-3600 UV-vis-NIR spectrophotometer, recording data across the 400-800 nm wavelength range.

Colorimetric quantification of NH_4^+

The quantification of converted NH_4^+/NH_3 was performed using a colorimetric method with indophenol blue. The procedure involved mixing 1 mL of the sampled electrolyte, diluted if needed, with 1 mL of 1 M NaOH solution containing 5% w/w salicylic acid and 5% w/w trisodium citrate. Then, 1 mL of 0.05 M NaClO and 0.1 mL of 1% w/w sodium nitroprusside ($C_5FeN_6Na_2O$) were added. After 2 hours, the absorbance was measured with a spectrophotometer, and the indophenol blue concentration was determined at 655 nm. The calibration curve was created using various NH_4Cl standards in 0.1 M PBS/$NaNO_3$, as shown in **Figure S3a-b**.

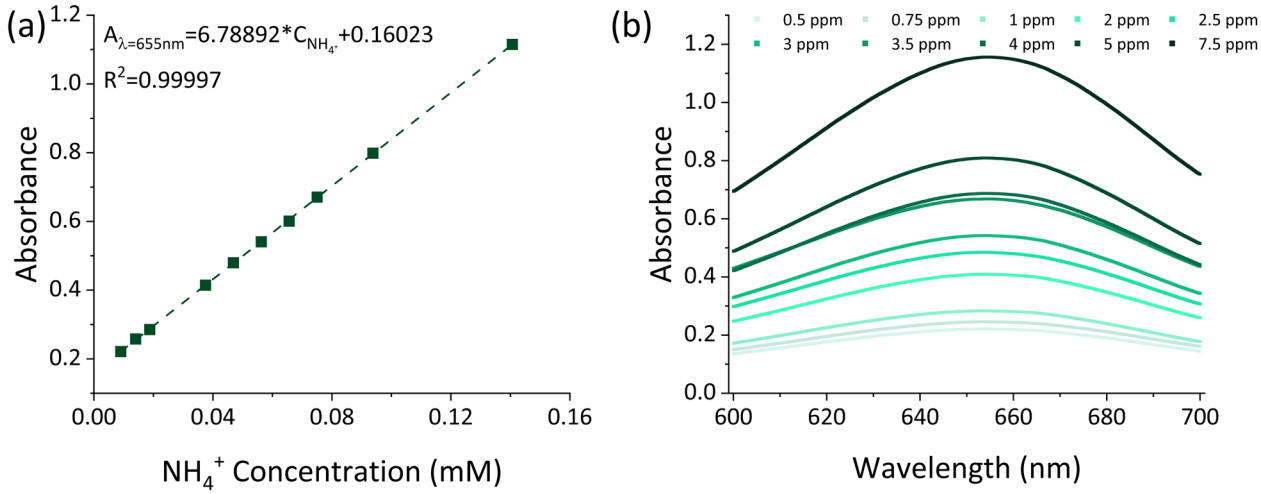

Figure S3. **a.** calibration curve of NH_4^+ in 0.1 M PBS/1M $NaNO_3^-$ electrolyte and the corresponding **b.** UV-vis spectra of the calibration standards.

Colorimetric quantification of NO_2^-

The Griess test was used to measure nitrite levels. The color reagent was made by dissolving 0.5 g of sulfanilamide and 0.5 g of N-1-naphtylethylenediamine dihydrochloride in 50 mL of DIW. To develop the sample color, 1 mL of appropriately diluted electrolyte was mixed with 2 mL of DIW and 1 mL of the Griess reagent. After 20 minutes, the absorbance of the sample was read at 540 nm. A calibration curve was generated using a series of $NaNO_2$ standards prepared in 0.1 M PBS/$NaNO_3$, measured as described (see **Figure S4a-b**).

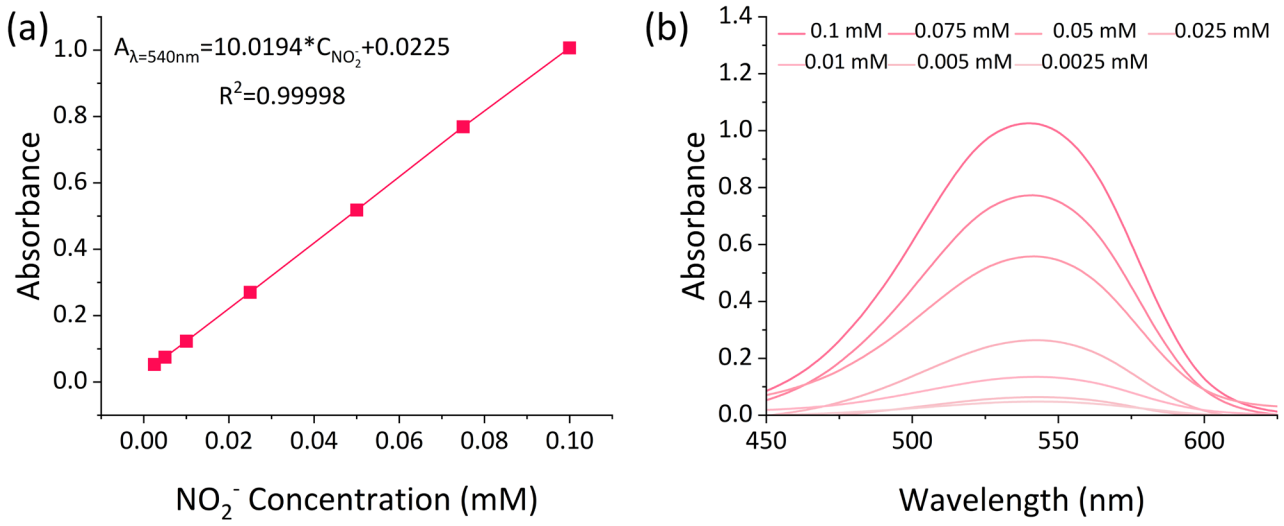

Figure S4. **a.** calibration curve of NO_2^- in 0.1 M PBS/1 M $NaNO_3$ electrolyte and the corresponding **b.** UV-vis spectra of the calibration standards.

4. Determination of NH_4^+ concentration by ^1H NMR

The concentration of electrochemically generated NH_4^+ was validated by ^1H NMR spectroscopy using a Bruker AVANCE III-500 spectrometer. For each measurement, 280 µL of electrolyte was mixed with 13 µL of concentrated H_2SO_4, 100 µL of DMSO-d_6, and 20 µL of 8.5 mM maleic acid as an internal standard. Water suppression was applied via pre-saturation prior to data acquisition. Quantitative calibration was performed using $^{15}NH_4^+$ standards, and the NH_4^+ concentration obtained by NMR was compared with that determined by the indophenol blue method.

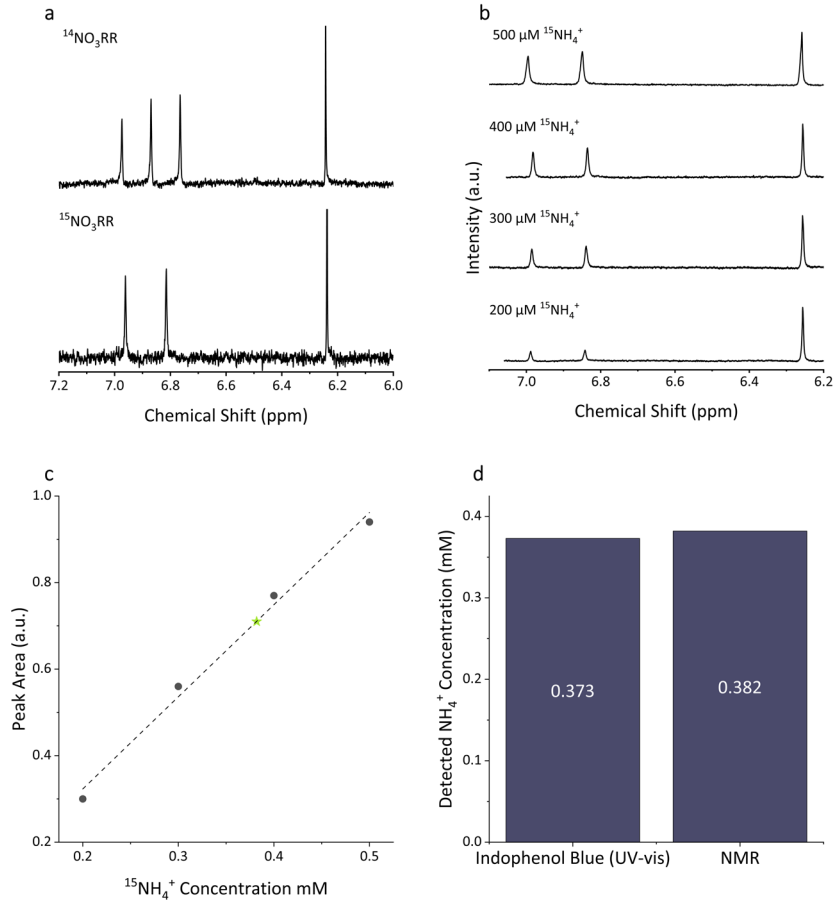

Figure S5. ^1H NMR validation and quantification of NH_4^+ produced during NO_3RR. **a.** ^1H NMR spectra of NH_4^+ generated from $^{14}NO_3^-$ and $^{15}NO_3^-$ reduction. **b.** ^1H NMR spectra of $^{15}NH_4^+$ calibration standards prepared at different concentrations using maleic acid as an internal standard. **c.** Calibration curve obtained from the integrated $^{15}NH_4^+$ peak area; the green marker symbolizes the NO_3RR sample. **d.** Comparison of NH_4^+ concentration determined by the indophenol blue method and quantitative ^1H NMR.

5. Complementary Data

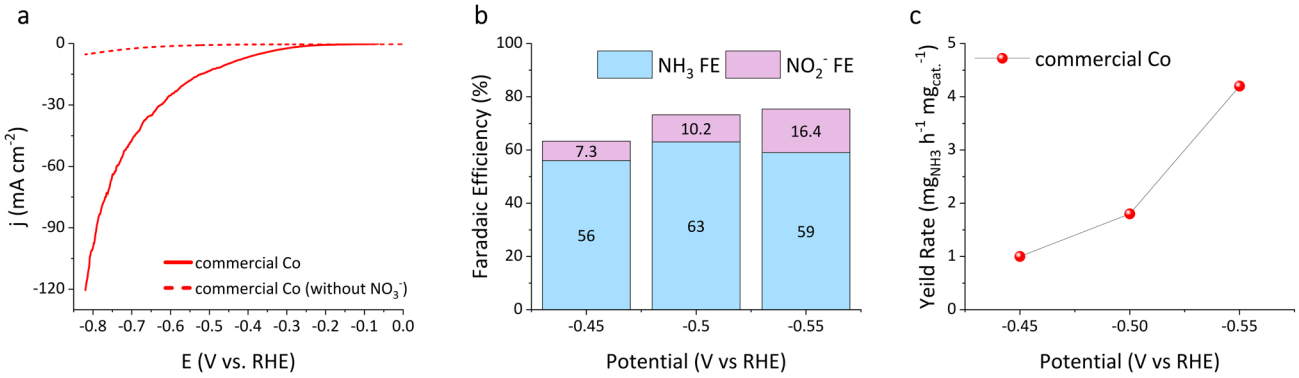

Figure S6. Electrocatalytic NO_3RR performance of commercial Co powder. **a.** LSV curves recorded in 0.1 M PBS with and without 1 M $NaNO_3$. **b.** NH_3 and NO_2^- Faradaic efficiencies at selected potentials. **c.** Corresponding NH_3 yield rates.

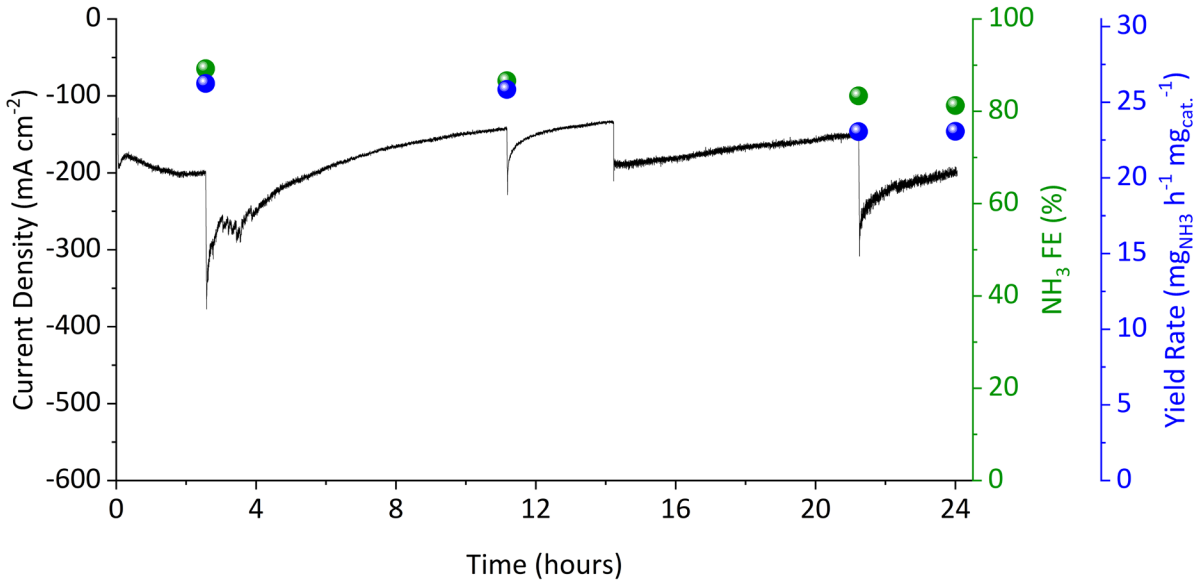

Figure S7. Long-term NO_3RR stability test of Co_2P/Co at −0.55 V vs. RHE. The black curve shows the current density over 24 h, while the green and blue markers show the NH_3 Faradaic efficiency and NH_3 yield rate, respectively.

Table S1. Benchmarking of NO_3RR performance for Co_2P, Co_2P/Co, commercial Co, and selected reported Co-based and transition-metal phosphide electrocatalysts.

catalyst type	potential V vs RHE	Electrolyte	NH_3 Yield Rate		J_{NH3}	FE	Ref.
			mg h^{-1} mg_{cat}^{-1}	mmol h^{-1} cm^{-2}	mA cm^{-2}	%	
Co_2P/Co	-0.55 V	0.1 M PBS + 1 M $NaNO_3$	21.3	0.652	-139	87	**This work**
Pristine Co_2P			3.8	0.115	-24.3	79	
Commercial Co			4.2	0.126	-26.8	59	
CoP@Co	-0.2 V	1 M KOH+0.5 M KNO_3	17.88	1.05	-149	96.70	[2]
CoP porous amorphous nanoshuttles	-0.5	0.5 M K_2SO_4+0.05 M KNO_3	19.28	0.163	-	94.24	[4]
Ti plate supported Co-P alloy film (Co-P/TP)	-0.6	0.2 M Na_2SO_4+200 ppm NO_3^-	-	0.0224 (416 μg h^{-1} cm^{-2})	-	93.6	[5]
CoP nanosheet arrays grown on carbon fiber cloth (CoP NAs/CFC)	-0.3	1 M KOH+ 1 M $NaNO_3$	96.9	9.56	-	~100	[6]
amorphoous Co-P@Ni foam	-0.3	1 M KOH + 1 M NO_3^-	49.4	9.33	2000	97.5	[7]
CoP nanorings (CoP NRs)	-0.5	0.5 M Na_2SO_4+50 mM $NaNO_3$	30.1	-	-	97.1	[8]
CoP@P-yeast	-0.25	1M NaOH+ 1M $NaNO_3$	33	-	-	67.6	[9]
CoP-CNS on copper foam	-1.03	1 M KOH+ 1M KNO_3	51.6	8.47	1860	88.6	[10]
Fe-doped CoP nanohoops (Fe-/CoP NHs)	-0.25 V	1 M KOH+50 mM KNO_3	27.6	-	-	93.3	[11]

Cu_3P/CoP	-0.9	0.1 M KOH+0.1M KNO_3	-	1.04	-	97.95	[12]
Ni_2P	-1.2 V vs Hg/HgO (~ -0.9 V_{RHE})	0.5 Na_2SO_4+ 80 mg/L NO_3^--N	0.95	0.16	-	99.2	[13]
Fe/Ni_2P	-0.4	0.2 K_2SO_4 + 50 mM KNO_3	2.09	0.245	-	94.3	[14]
Fe_2P	-0.55	0.5 M NaOH+ 0.2 M NO_3^-	-	0.25	-	96	[15]
amorphous cobalt phosphate in carbon matrix (Co-P-O/C)	-0.2	1 M KOH + 0.1 M KNO_3	20.14	0.401		97	[16]
np-$Co_{1.34}Cu_{0.66}P$	-0.3	1M KOH+ 0.1 M $NaNO_3$	-	1.8	-	93.38	[17]

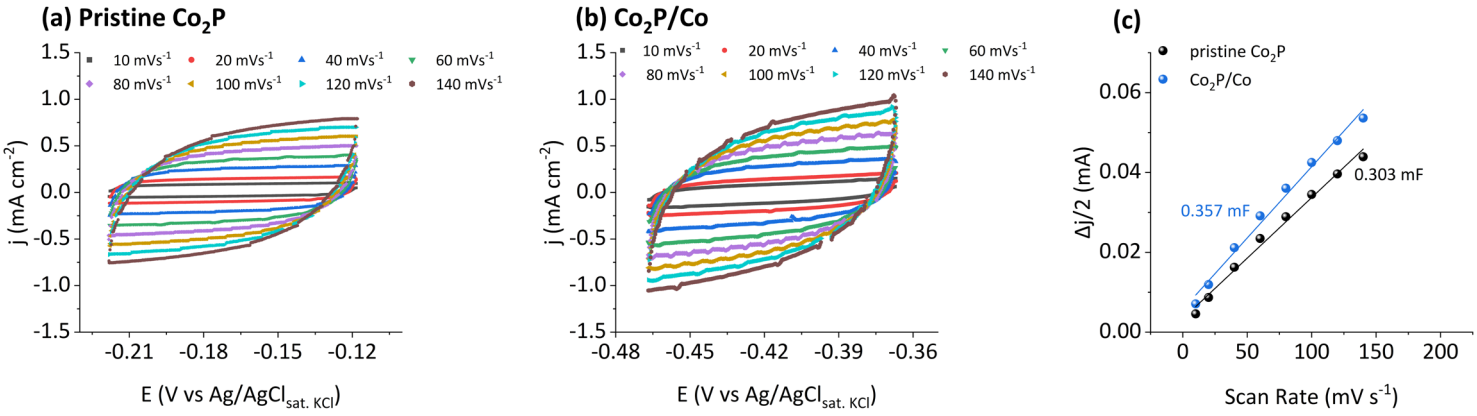

Figure S8. Double-layer capacitance (C_{dl}) measurements: cyclic voltammograms of **a.** pristine Co_2P, **b.** Co_2P/Co samples and **c.** the corresponding mean mid-current density vs. scan rate linear trends.

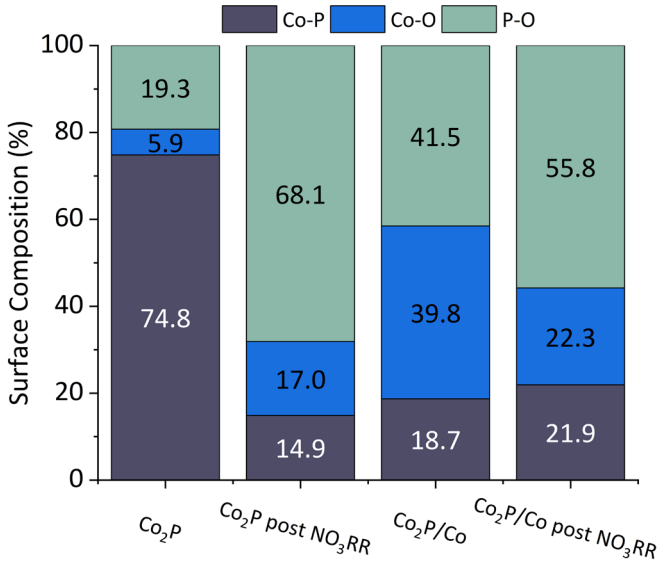

Figure S9. Quantitative XPS surface composition of Co_2P and Co_2P/Co before and after NO_3RR.

Table S2. In situ ATR-FTIR peak positions corresponding to the detected signals in Co_2P and Co_2P/Co spectra.

Peak position (cm^{-1})	Observed in	Assignment	References
1130–1150	Co_2P/Co	*N-O vibration of adsorbed NO_x species	[10, 18]
1220–1260	Co_2P	$*NO_2^-$	[18, 19]
1290–1300	Co_2P	NH_2 wagging mode	[20]
1340–1360	Co_2P/Co	NO_3^- (aq)	[19]
1440–1460	Both	N-H bending	[20]
1480–1500	Co_2P	NH_3/NH_4^+	[21, 22]
1510–1540	Both	*NH	[23]
1585–1590	Co_2P	*NO	[24]
1600–1660	Both	H-O-H bending (adsorbed H_2O)	[19, 25]

References

1. Bandyopadhyay, D., et al., *Full water splitting electrolyzed by Cu–Co bimetallic phosphides.* ACS Appl. Energy Mater., 2023. **6**(21): p. 10987-10995.
2. Yang, K., et al., *Unveiling the reaction mechanism of nitrate reduction to ammonia over cobalt-based electrocatalysts.* J. Am. Chem. Soc., 2024. **146**(19): p. 12976-12983.
3. Yang, J., et al., *Synthesis and characterization of cobalt hydroxide, cobalt oxyhydroxide, and cobalt oxide nanodiscs.* J. Phys. Chem. C., 2010. **114**(1): p. 111-119.
4. Jia, Y., et al., *Efficient nitrate-to-ammonia electroreduction at cobalt phosphide nanoshuttles.* ACS Appl. Mater. Interfaces, 2021. **13**(38): p. 45521-45527.
5. Li, Z., et al., *High-efficiency nitrate electroreduction to ammonia on electrodeposited cobalt–phosphorus alloy film.* Chem. Commun., 2021. **57**(76): p. 9720-9723.
6. Ye, S., et al., *Elucidating the activity, mechanism and application of selective electrosynthesis of ammonia from nitrate on cobalt phosphide.* Energy Environ. Sci., 2022. **15**(2): p. 760-770.
7. Fan, J.-L., et al., *Electrochemical reduction of nitrate to ammonia on ultra-stable amorphous Co–P electrocatalyst.* J. Mater. Chem. A, 2024. **12**(31): p. 20077-20087.
8. Hong, Q.-L., et al., *Cobalt phosphide nanorings towards efficient electrocatalytic nitrate reduction to ammonia.* Chem. Commun., 2021. **57**(88): p. 11621-11624.
9. Ojima, Y., et al., *Cobalt phosphide-loaded biochar synthesis using phosphate-accumulating yeast and its application as an electrocatalyst.* Biotechnology Reports, 2025. **45**: p. e00874.
10. Fan, K., et al., *Active hydrogen boosts electrochemical nitrate reduction to ammonia.* Nat. Commun., 2022. **13**(1): p. 7958.
11. Hong, Q.-L., et al., *Iron-doped cobalt phosphide nanohoops for electroreduction of nitrate to ammonia.* Inorg. Chem., 2022. **61**(36): p. 14397-14402.
12. Liu, P., et al., *Cu_3P/CoP Heterostructure for Efficient Electrosynthesis of Ammonia from Nitrate Reduction Reaction.* ACS Appl. Mater. Interfaces, 2024. **17**(1): p. 980-990.
13. Yao, Q., et al., *Selective electrocatalytic reduction of nitrate to ammonia with nickel phosphide.* ACS Appl. Mater. Interfaces., 2021. **13**(26): p. 30458-30467.
14. Zhang, R., et al., *Efficient ammonia electrosynthesis and energy conversion through a Zn-nitrate battery by iron doping engineered nickel phosphide catalyst.* Adv. Energy Mater., 2022. **12**(13): p. 2103872.
15. Chouki, T., et al., *Highly active iron phosphide catalysts for selective electrochemical nitrate reduction to ammonia.* J. Environ. Chem. Eng., 2023. **11**(2): p. 109275.
16. Lei, F., et al., *Amorphous cobalt phosphate incorporated in carbon matrix as an efficient pre-catalyst for promoted electrosynthesis of ammonia.* J. Mater. Chem. A, 2023. **11**(31): p. 16854-16859.
17. Huang, Y., et al., *Enhanced Nitrate Reduction Performance of Cu-Doped Nanoporous Co_2P Electrocatalyst.* Nanomater., 2025. **15**(10): p. 753.
18. Dai, Y., et al., *Tandem Active Sites in Cu/Mo-WO_3 Electrocatalysts for Efficient Electrocatalytic Nitrate Reduction to Ammonia.* Adv. Funct. Mater., 2025. **35**(20): p. 2420282.
19. Da Cunha, M., M. Weber, and F.C. Nart, *On the adsorption and reduction of NO_3^- ions at Au and Pt electrodes studied by in situ FTIR spectroscopy.* J. Electroanal. Chem., 1996. **414**(2): p. 163-170.
20. Yao, Y., et al., *A spectroscopic study of electrochemical nitrogen and nitrate reduction on rhodium surfaces.* Angew. Chem. Int. Ed., 2020. **132**(26): p. 10565-10569.

21. Dong, J.H., et al., *Engineering Ce promoter to regulate H* species to boost tandem electrocatalytic nitrate reduction for ammonia synthesis.* Adv. Funct. Mater., 2025. **35**(25): p. 2422025.
22. Li, S., et al., *Localized enriching nitrate/proton on reconstituted Fe nanoparticles boosting electrocatalytic nitrate reduction to ammonia.* J. Energy Chem., 2025. **103**: p. 682-691.
23. Zhang, M., et al., *Hydration-effect Boosted Active Hydrogen Facilitates Neutral Ammonia Electrosynthesis from Nitrate Reduction.* Adv. Funct. Mater., 2025. **35**(2): p. 2413070.
24. Zhang, S., et al., *Concurrently Selective Electrosynthesis of Ammonia and Glycolic Acid Over Cathodic Single-Atom Cobalt and Anodic PdNi Alloying Catalysts.* Adv. Funct. Mater., 2025. **35**(6): p. 2415046.
25. Yesudoss, D.K., et al., *Time-Resolved Fourier Transform Infrared Spectroelectrochemical Investigation of Nitrate Reduction to Ammonia.* ACS Energy Lett., 2025. **10**(4): p. 1688-1699.